J. Fluid Mech. (2013), *vol.* 717, *pp.* 484–513.
doi:10.1017/jfm.2012.588

On the scaling of air layer drag reduction

Brian R. Elbing[1,†], Simo Mäkiharju[2], Andrew Wiggins[3], Marc Perlin[3], David R. Dowling[2] and Steven L. Ceccio[2,3]

[1]Applied Research Laboratory, Pennsylvania State University, University Park, PA 16804, USA

[2]Mechanical Engineering, University of Michigan, Ann Arbor, MI 48109, USA

[3]Naval Architecture and Marine Engineering, University of Michigan, Ann Arbor, MI 48109, USA

(Received 19 February 2012; revised 19 November 2012; accepted 26 November 2012; first published online 1 February 2013)

Air-induced drag reduction was investigated on a 12.9 m long flat plate test model at a free stream speed of 6.3 m s^{-1}. Measurements of the local skin friction, phase velocity profiles (liquid and gas) and void fraction profiles were acquired at downstream distances to 11.5 m, which yielded downstream-distance-based Reynolds numbers above 80 million. Air was injected within the boundary layer behind a 13 mm backward facing step (BFS) while the incoming boundary layer was perturbed with vortex generators in various configurations immediately upstream of the BFS. Measurements confirmed that air layer drag reduction (ALDR) is sensitive to upstream disturbances, but a clean boundary layer separation line (i.e. the BFS) reduces such sensitivity. Empirical scaling of the experimental data was investigated for: (*a*) the critical air flux required to establish ALDR; (*b*) void fraction profiles; and (*c*) the interfacial velocity profiles. A scaling of the critical air flux for ALDR was developed from balancing shear-induced lift forces and buoyancy forces on a single bubble within a shear flow. The resulting scaling successfully collapses ALDR results from the current and past studies over a range of flow conditions and test model configurations. The interfacial velocity and void fraction profiles were acquired and scaled within the bubble drag reduction (BDR), ALDR and transitional ALDR regimes. The BDR interfacial velocity profile revealed that there was slip between phases. The ALDR results showed that the air layer thickness was nominally three-quarters of the total volumetric flux (per unit span) of air injected divided by the free stream speed. Furthermore, the air layer had an average void fraction of 0.75 and a velocity of approximately 0.2 times the free stream speed. Beyond the air layer was a bubbly mixture that scaled in a similar fashion to the BDR results. Transitional ALDR results indicate that this regime was comprised of intermittent generation and subsequent fragmentation of an air layer, with the resulting drag reduction determined by the fraction of time that an air layer was present.

Key words: drag reduction, gas/liquid flows, multiphase flows

1. Introduction

Skin-friction drag constitutes a significant portion of the total resistance for nearly all transportation systems moving in a fluid. Thus, due to the continual desire to reduce energy consumption and the resulting environmental impact, skin-friction drag reduction techniques have been widely studied for several decades. Some techniques

† Email address for correspondence: bre11@psu.edu

explored for hydrodynamic skin-friction drag reduction include the addition of a polymer solution (White & Mungal 2008), superhydrophobic surface coatings (Martell, Perot & Rothstein 2009; Davis & Lauga 2010; Rothstein 2010; Lee & Kim 2011) and air cavities (Amromin *et al.* 2006; Matveev, Burnett & Ockfen 2009; Lay *et al.* 2010; Matveev & Miller 2011). Another technique, which is the focus of the current study, involves the injection of gas (typically air) into the near-wall region of a liquid (water) turbulent boundary layer (TBL). When implemented at relatively low or high gas fluxes, this air-injection method is termed bubble drag reduction (BDR) and air layer drag reduction (ALDR), respectively. While the majority of studies to date have focused on BDR, ALDR has been demonstrated on both smooth and rough walls at downstream-distance-based Reynolds numbers exceeding 130 million (Elbing *et al.* 2008). The current study extends these previous findings to document the effects that vortex generators and free stream flow unsteadiness have on ALDR to assess its robustness for surface ship applications. Furthermore, the current work develops scalings that collapse void fraction profiles, the gas–liquid interface-velocity profiles and measurements of the critical air flux required to transition from BDR to ALDR. In particular, the void fraction and interface velocity profile measurements span the range of flow-morphologies arising from BDR, transitional ALDR and fully established ALDR with and without flow perturbations. Previously these measurements were not possible (especially in the transitional ALDR regime) because of experimental limitations; however, these have been overcome with the introduction of a free surface within the test section of the flow facility used for this study.

While the bulk of the work reported here is related to ALDR, it is informative to include a brief review of some of the historical work related to BDR that motivated this study. Readers interested in a more complete review of BDR are directed to the reviews of Merkle & Deutsch (1992) and Ceccio (2010). Numerous studies have been conducted since the seminal BDR work of McCormick & Battacharyya (1973) and Bodgevich & Evseev (1976). These studies investigated the influence of various flow and injection parameters on BDR, and measured drag reduction exceeding 80 % in laboratory settings.

While the underlying physical mechanisms of BDR are not fully understood, it is generally agreed that bubbles reduce turbulent momentum exchange in the buffer region of the TBL. Most of the proposed drag reduction mechanisms involve a decrease in the near-wall Reynolds stress ($-\rho\langle u'v'\rangle$), where ρ is the fluid density and u' and v' are the streamwise and wall-normal velocity fluctuations, respectively. One suggested mechanism for this reduction is a decrease in the bulk density, which would suggest that drag reduction would scale with the near-wall void fraction. This scaling is supported by the experimental results of Elbing *et al.* (2008). Another mechanism suggested by Lumley (1973, 1977) is that the bubbles increase the local viscosity in the sublayer and buffer region resulting in a suppression of the near-wall velocity fluctuations, which has been supported experimentally (Pal, Deutsch & Merkle 1989) and computationally (Druzhinin & Elghobashi 1998; Ferrante & Elghobashi 2004). Conversely, Nagaya *et al.* (2001) experimentally found that the turbulent fluctuations increased with gas injection. Thus, an alternative mechanism suggested was that the bubbles decorrelate the streamwise and wall-normal velocity fluctuations resulting in a decrease in the Reynolds stress. These mechanisms as well as mechanisms related to bubble splitting and deformation (Meng & Uhlman 1998; van den Berg *et al.* 2005; Lu, Fernández & Tryggvason 2005) are supported experimentally and computationally, which suggests that multiple mechanisms are simultaneously active. Thus, it is not surprising that a universal scaling law has yet to be developed for BDR.

In spite of uncertainty about the physical mechanisms, the success of BDR in laboratory-scale experiments (models typically less than 1 m long at downstream-distance-based Reynolds numbers at or below 10^7) motivated the extension of BDR measurements to larger scales. This is critical as the Reynolds number scaling of turbulent boundary layers is a non-trivial problem (Klewicki 2010) that is further complicated with multiple phases. One set of experiments used long (12–50 m), slender flat-bottom ship models (Watanabe, Masuko & Shirose 1998; Kodama, Kakugawa & Takahashi 1999; Kodama *et al.* 2002) and full-scale sea trials (Kodama *et al.* 2000; Nagamatsu *et al.* 2002; Kodama *et al.* 2006). The most recent sea trials produced an overall power savings of a few per cent. The first commercial production of bulk carriers that use an air injection drag reduction scheme (MALS, Mitsubishi Heavy Industries) was reported recently (Konrad 2011). Three grain carriers are scheduled to be built that will measure 237 m long, 40 m wide and 12.5 m draft (at design condition). With limited information it appears that the air lubrication scheme will produce transitional air layers, which could reduce CO_2 emissions by 25 % (value reported in news releases).

These ship-scale advances are encouraging, but due to the complexity of sea trials and minimal release of data from the commercial efforts, physical insights are not readily gained from such studies. For this we revert to the largest-possible laboratory experiments. The work of Sanders *et al.* (2006) and Elbing *et al.* (2008) produced experimental data at comparable model lengths to the current study within a laboratory setting, which enabled high-fidelity, high-Reynolds-number BDR measurements. These results indicated that beyond a couple metres downstream of the air-injection location, BDR produces minimal drag reduction because shear forces and turbulent motions remove bubbles from the near-wall region. Furthermore, investigation of compound injection (injecting gas from multiple downstream locations) produced either negligible change or a decrease in drag reduction relative to injection of the equivalent volume from a single location. Thus, due to the relatively poor downstream persistence of BDR, ALDR remains of interest in spite of the larger required air fluxes.

ALDR occurs when a continuous or nearly continuous layer of air separates the solid surface from the flowing liquid resulting in a substantial skin-friction drag reduction, here defined as more than 80 % relative to when such an air layer is absent. The primary advantage of ALDR compared with BDR is that to date no degradation with increasing downstream distance has been observed with ALDR. While ALDR results have been inadvertently reported in several past studies (Madavan, Deutsch & Merkle 1985; Kodama *et al.* 2002; Sanders *et al.* 2006), only recently have there been studies focused specifically on ALDR. The basic features of ALDR are identified by Elbing *et al.* (2008). The key findings from that study are: (i) stable air layers can form at speeds to 15.3 m s^{-1} (experimental air flux limitations prevented ALDR measurements at higher speeds) with no decrease in drag reduction over the entire model length ($\sim$10 m); (ii) the required air flux is approximately proportional to the square of the free stream speed; (iii) surface tension aids in stabilizing the air layer (i.e. decreased surface tension requires larger air fluxes); (iv) ALDR can be achieved on significantly roughened surfaces but larger air fluxes are required at a given speed; and (v) inflow disturbances can adversely impact the formation and stability of the air layer, but such a sensitivity can be mitigated through the use of a clean boundary layer separation line prior to the air injection location.

The final observation was made with no quantitative analysis as it was not a focus of that study. Consequently, an effort was made within the current work to produce controlled perturbations to the incoming boundary layer immediately upstream

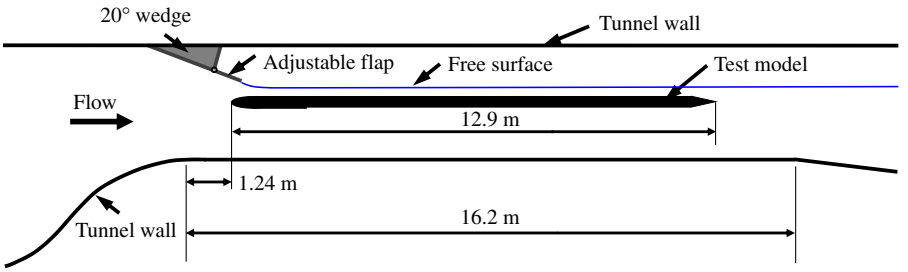

FIGURE 1. (Colour online) Elevation side view of the LCC test section modified with the 20° wedge. The test model was positioned slightly below the vertical centreline. The nominal position of the free surface is also shown for reference. (Not to scale.).

of injection. A clean line of separation was produced with a backward facing step (BFS) and air injected into the flow at the base of the BFS formed the air layer. The perturbations were produced with a row of vortex generators positioned at various angles of attack (AoAs). In addition, the current work investigates scaling of the critical air flux for ALDR, mean void fraction profiles and gas/liquid interface velocity profiles. The remainder of this paper is organized as follows: § 2 describes the experimental methods employed; in § 3 we present and discuss our results; and § 4 provides a summary of this work and the conclusions drawn from it.

2. Experimental methods

2.1. *Test facility*

The experiments were conducted in the US Navy's William B. Morgan large cavitation channel (LCC), the world's largest low-turbulence recirculating water tunnel. The LCC has a volume of 5300 m^3 with a test section that measures 13 m (length) × 3.05 m (width) × 3.05 m (height). (See Etter *et al.* (2005) for additional LCC facility details.) For the current study, the LCC and its standard operating procedures were modified to facilitate the formation of a stable free surface within the test section (additional details on facility modifications provided in Mäkiharju (2012)). The free surface was necessary to permit air injected beneath the test model to escape from the LCC and thereby allow test conditions to be maintained for long periods of time (in excess of an hour) with minimal variation in tunnel pressure. In previous LCC air-injection experiments (Sanders *et al.* 2006; Elbing *et al.* 2008; Lay *et al.* 2010), the test time for a fixed condition was limited due to the rise in tunnel pressure caused by the accumulation of air within the closed-loop-configured LCC.

To produce a free surface in its test section, a triangular wedge was attached to the top of the tunnel immediately upstream of the test section and it projected downward and downstream into the test section (see figure 1). While a portion of the wedge could be articulated to vary the angle, during the current experiment it was fixed at a constant 20° angle with respect to the horizontal. The wedge angle was monitored with an inclinometer (SCA121T-D03, VTI Technologies) and was simultaneously recorded with the other flow diagnostics. The variation in wedge angle during the experiment was less than 0.1°, but the calibration had an uncertainty of ∼6 %. The wedge spanned the test section width and protruded downward 0.97 m from the channel top. The water depth within the test section varied depending on the initial fill height and channel impeller rotation rate. However, at zero speed, the initial water depth within

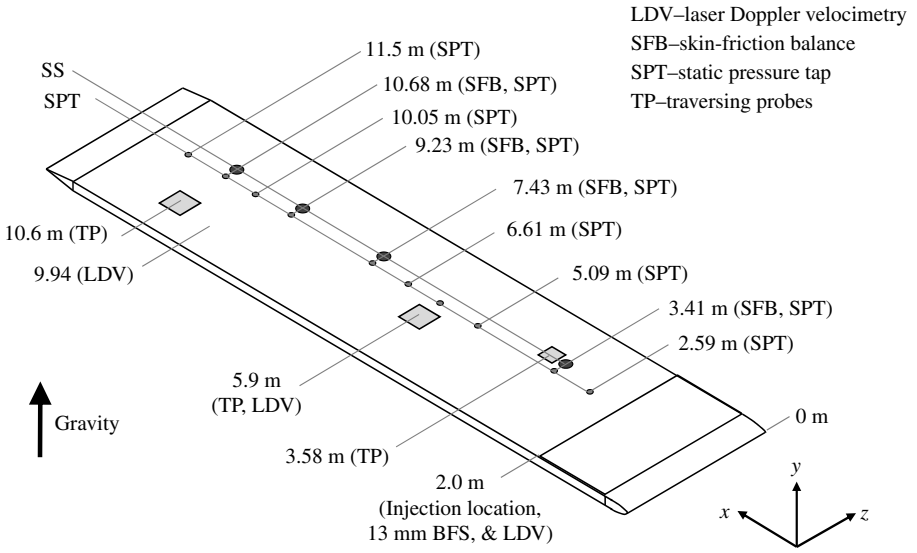

FIGURE 2. Schematic of the test model with gravity oriented upward (i.e. showing the working surface). The locations of the instrumentation used and the BFS/injection position are shown.

the test section was 2.8 ± 0.03 m; at steady state (17.5 rpm) the depth decreased to 2.0 ± 0.01 m. When at speed, the free surface extended through the test section and into the diffuser where a hydraulic jump occurred. The water depth was regularly monitored with a simple scale fixed to an acrylic window near the midpoint of the LCC test section ($X \sim 5.9$ m).

2.2. *Experimental platform*

The test model was a 12.9 m (length) $\times$ 3.05 m (width) $\times$ 18 cm (depth) rigid flat plate that has been used in several previous studies investigating high-Reynolds-number turbulent boundary layers (Oweis *et al.* 2010), air-induced drag reduction (Sanders *et al.* 2006; Elbing *et al.* 2008; Lay *et al.* 2010) and polymer drag reduction (Winkel *et al.* 2009; Elbing *et al.* 2010, 2011). It spanned the LCC test section width, had the working surface facing downward and was mounted slightly below the LCC test section centreline. The coordinate system used has the X origin at the model leading edge with X increasing downstream, and the Y origin at the model surface with Y increasing perpendicularly into the flow and to the model surface. The third Cartesian coordinate, Z, extends in the spanwise direction completing a right-handed coordinate system. For the current experiment the flat-plate model was modified with a 13 mm BFS at the injection location ($X = 2.0$ m). Figure 1 provides a side-view schematic of the test model positioned within the LCC test section, and figure 2 shows a model schematic that depicts the instrument suite.

The BFS was fabricated from a stainless steel plate that spanned the model width and extended 1.63 m upstream of the injection location. A brass section extending from the model leading edge to $X = 0.37$ m smoothly faired the BFS with the model leading edge in an elliptical profile. The flat section length (1.63 m) upstream of injection was selected such that there were over 100 boundary layer thicknesses between the downstream end of the elliptical section and the injection location. Air

was injected into the flow through a 6.4 mm slot along the base of the BFS. The opening was connected to a 2.5×10^{-2} m^3 rectangular cavity embedded within the step, which was supplied with air from the injection/manifold arrangement described by Elbing *et al.* (2011). The cavity and BFS promoted spanwise uniformity of the injected air, which was monitored throughout testing *via* flow visualization over the entire model working surface.

The BFS causes a disturbance to the incoming boundary layer that persists downstream and could impact the formation of a stable air layer. This boundary layer disturbance is a well-known phenomenon that has been studied by numerous researchers, including Kim, Kline & Johnston (1980). Kim *et al.* showed that the near-wall region recovers the mean velocity within ∼16 step heights downstream of the BFS, full recovery of the mean velocity profiles require longer distances and near the reattachment zone (∼7 step heights downstream) there is a maximum in turbulent intensity that rapidly decays after reattachment. In the current study a velocity profile was acquired at $X = 2.09$ (included in figure 8), which is nominally seven step heights downstream of the BFS. This profile shape is consistent with previously measured profiles near the reattachment point. The next velocity profile acquired was located 310 step heights downstream from the BFS and is in excellent agreement with the velocity profile upstream of the BFS. The first measurement of shear stress, void fraction or interfacial velocity was acquired at 111 step heights downstream of the BFS, and this location is an order magnitude further downstream than the region expected to have the greatest impact from the BFS (i.e. the location of maximum turbulent intensity). However, it is important to stress that even though the measurement locations are beyond the region impacted by the BFS, the BFS disturbance could still impact the results due to the potential influence on the transition from BDR to ALDR.

Past ALDR work (Elbing *et al.* 2008) indicated that the ability to form stable air layers was dependent on the turbulence level in the incoming flow. Thus, in the current study, additional flow perturbations were intentionally produced immediately upstream of the injection location with 10 vortex generators (VGs) evenly spaced in the spanwise direction and centred 8.9 cm upstream of the BFS. The spacing between VGs was greater than 10 boundary layer thicknesses, thus isolating the disturbance from each VG at the injection location. The generators were symmetrical foils that were oriented perpendicular to the main test model body. The VGs were fabricated from brass, measured 9.5 cm (streamwise length) × 3.2 mm (spanwise thickness) × 1.4 cm (wall-normal height), had a 4:1 ellipse at the leading edge and a 15° truncated wedge at the tail. The full boundary layer thickness (δ) at the VG position was nominally 25 mm, which sets the VG height at approximately 0.56δ. Conventional VGs have a height that is approximately equal to δ, but Yao, Lin & Allan (2002) showed that low-profile VGs can produce similar levels of streamwise vorticity while permitting greater AoAs without separation, which was desirable for this experiment. The VGs were designed by requiring the circulation of their vortical wakes to produce a vertical velocity at the air-layer with sufficient kinetic energy to raise the air–water interface to the test model wall. This required circulation was used with the data presented by Yao *et al.* (2002) to select the dimensions and maximum AoA. During testing the VG AoA could be adjusted between 0 and 10° to generate streamwise vortices of varying strength in the incoming flow.

2.3. *Instrumentation*

Local skin-friction measurements were acquired at four streamwise locations ($X =$ 3.41, 7.43, 9.23 and 10.68 m) with floating-plate-type drag balances. The floating

plates were 0.79 cm thick, had a 15.2 cm diameter, fabricated from 17-4pH stainless steel and had a 60 ± 20 μm annular gap between the plate and surrounding housing. The plate was fixed rigidly to a beryllium copper flexure that was instrumented with a full Wheatstone bridge of semiconductor strain gauges. A schematic of a sensor is provided by Elbing *et al.* (2010) and calibration details can be found in Elbing *et al.* (2008). The typical uncertainty was approximately $\pm 8\,\%$, which is slightly higher than the previously reported accuracy using similar sensors due to a relatively small number of repeated conditions. The balances were used to directly measure skin-friction at the wall. Per cent drag reduction ($\%DR$),

$$\%DR = \left(1 - \frac{\tau_w}{\tau_{wo}}\right) \times 100, \tag{2.1}$$

was determined by comparing measurements with and without air injection. Here τ_w and τ_{wo} are the wall shear stress with and without injection, respectively. The no-injection skin friction was determined from a minimum of ten speed ramps from zero to the test speed, while the injection skin friction was determined from a minimum of three repeated tests with air injection.

Three instrument probes were mounted on a wall-normal traversing system at three streamwise locations ($X = 3.58, 5.87$ and 10.61 m). The three traversing systems were identical, with a time-of-flight (ToF) probe, electrical impedance point probe and Pitot-static probe. The spanwise spacing between each probe was 26 mm, as shown in figure 3, and each probe had a 3.2 mm outer diameter. The traverse system motor (Sigma 5 SGMAV-04A3A61, Yaskawa) was enclosed within the test model in a watertight anodized aluminum enclosure and the controller (SGDV-2R8F11A, Yaskawa) input was provided through a LabView interface. The motor turned a stainless steel gear mechanism, which in turn precisely positioned the probes within the flow. The actual probe positions were verified periodically with direct measurements throughout the duration of the experiment. Pre- and post-experiment testing of the positioning system confirmed that there was negligible movement in the system when holding position. The electronic components used for the ToF and impedance point probes were similar to those used by Elbing *et al.* (2008), with any differences stated below.

The ToF probes were composed of five conducting rings with a nominal 3.2 mm outer diameter and a streamwise spacing of 5.1 mm between each ring on a non-conducting Garolite rod. The upstream ring was 12.7 mm downstream from the rod's tip, which was machined to an elliptical shape. Each conducting ring was fabricated by machining a 0.5 mm wide groove into the non-conducting rod, wrapping a bare 32 gauge wire within the groove and then filling the groove with highly conductive silver epoxy. Finally the rings were re-machined and polished to ensure that the surface was smooth and longitudinally flat.

The ToF probe just described was used as follows (configuration schematically provided in the lower inset of figure 3): two electrode pairs with source locations spaced 10.2 mm in the streamwise direction had different supply voltage frequencies, which allowed a lock-in-amplifier (SR830 DSP, Stanford Research Systems) to isolate each signal. As the source frequency was used to decipher the individual signals, a single return line could be used for the receiver electrode. Thus, the first, third and fifth conducting rings were wired together and used as the receiver electrodes for both the upstream and downstream electrode sources (i.e. the second and fourth conducting rings, respectively). Each signal was extremely sensitive to the passage of bubbles, which allowed the interfacial velocity of the passing bubbles to be determined

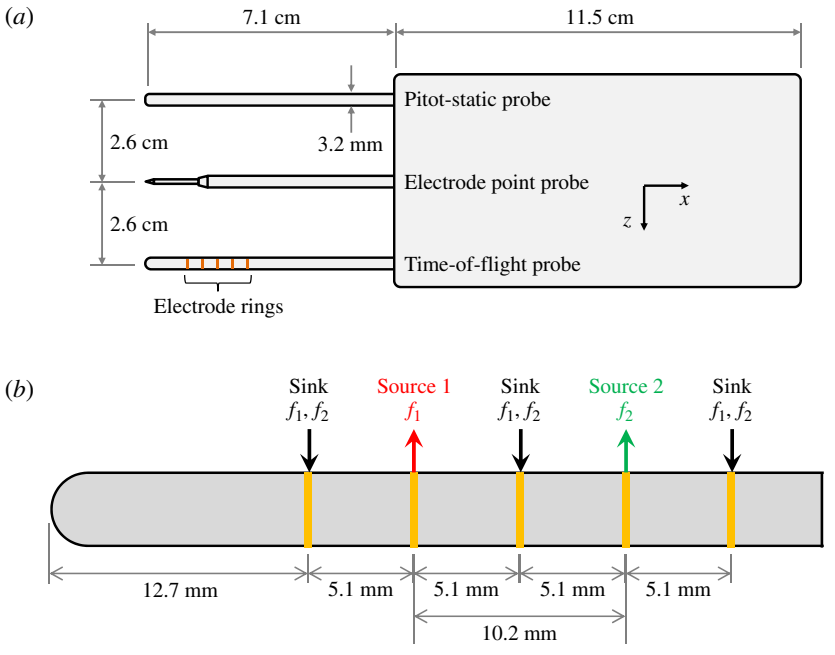

FIGURE 3. (Colour online) (*a*) Schematic of the traversing system with the three probes (Pitot-static, electrical impedance point and ToF probes). The probes were traversed in the wall-normal direction (Y). (*b*) Enlarged schematic of the ToF probe showing the two source electrode rings, which supplied an AC voltage at separate frequencies ($f_1 \neq f_2$). The three other rings were sinks that received signals influenced from either source, but were separated for processing with use of a narrow-band frequency filter.

via cross-correlation of the two signals. The interfacial velocity was determined from the source spacing (10.2 mm) divided by the shifted time that produced the maximum cross-correlation peak. A minimum of 10 independent 0.2 s measurements were averaged to produce the results presented.

The second probe was a point electrical impedance probe, which consisted of two electrodes produced from a 1.1 mm outer diameter rigid coaxial cable. The electrode was supported by a 3.2 mm outer diameter brass rod. The centre wire of the coaxial cable was used as the source electrode and was exposed to the boundary layer at the upstream probe tip. The coaxial cable shielding purposely was exposed slightly downstream from the leading edge, and served as the receiver electrode. The leading edge was machined conically with a nominal 60° included angle. The influence volume for each electrical impedance point was nominally a sphere of radius 1–2 mm around the probe tip. The influence volume was estimated by determining the distance from the probe that a non-conducting object causes a significant signal change. It should be noted that the actual influence volume at any point in time is dependent on the flow topology. For example the measured void fraction would be unity if a small bubble completely encased the centre electrode.

While electrical impedance probes are extremely sensitive to the air–water ratio within their influence volume, the primary challenge of using these probes for measurements of void fraction is converting the received signal to an actual void fraction. As noted above, the topology of the flow field has a significant impact on

the response of the electrical impedance probe. There are two extreme flow topologies, uniformly distributed or stratified, that should be considered in the analysis. If it is assumed that the probe measures a uniformly distributed bubbly mixture, then the measured impedance can be used to compute a void fraction following the analysis provided by Elbing *et al.* (2008) for the given circuit. Conversely, if the flow is assumed stratified locally (i.e. a single fluid is present over the influence volume), then each measurement is assumed influenced by only air or water and the mean void fraction is a time averaged binary signal. Note that the required duration of the measurement must be long relative to the time scale associated with the slug passage to produce an accurate measure of the void fraction. As both topologies are possible in the given setup, the raw data were reduced twice, applying each assumption separately. There was no difference in profile shape when processing with either method. The difference in measured void fraction was typically within 10 %, but there were larger outliers when the mixture was nearly pure air or water. The void fraction results shown are the average of the two data-reduction methods. It should also be noted that the current circuit was modified from that used by Elbing *et al.* (2008) with the reference resistor positioned between the voltage source and the electrode pair. This configuration introduces a greater sensitivity to the stray capacitance in the system, and consequently could cause increased uncertainty in the final results when assuming a bubbly mixture. This was investigated by performing a sensitivity analysis on the results with varying stray capacitance levels, and has been considered in the void fraction uncertainty, approximated at 10 %. The void fraction uncertainty was estimated from the observed scatter between: (i) individual test runs; (ii) different processing methodologies (i.e. binary/mixture models, simplified circuit analyses and computations using the real part, imaginary part or magnitude of the reference voltage); and (iii) comparing point probe measurements to ToF electrode results. The nominal void fraction uncertainty of 10 % was dependent on the void fraction levels. In general, near to zero void fraction (i.e. pure water), this uncertainty was less than 10 % while this uncertainty near a void fraction of one (i.e. pure air) was closer to 15 %.

The signal voltages in air and water were measured daily. The reference resistor for each circuit had a nominal resistance of 1000 Ω. The circuit was excited with a 5 VAC signal at a frequency of 41, 30 and 13 kHz for the probe traverses located at $X = 3.58, 5.87$ and 10.6 m, respectively. Typically the signals were sampled at 50 kHz, although for a subset of conditions the sampling rate was reduced as low as 10 kHz. The reduced sampling rate was used to increase the sampling period, which was typically one second, but the extended samples were as long as 30 s. The longer sampling periods were required due to the nature of the transitional ALDR regime, which exhibited irregular changes between air and water. This supports the conjecture that the transitional regime is in fact an unstable border between the distributed and stratified topologies.

The third probe on each traversing system was a Pitot-static probe (166 series 173839-00, Dwyer), which provided the local stagnation (p_{stag}) and static (p_{stat}) pressures. The pressure difference was recorded with a differential pressure transducer (PX2300-DI10, Omega; Model 230, Setra). If the void fraction is known, either from the electrical impedance measurement or in the absence of air, the pressure

difference ($p_{stag} - p_{stat}$) can be used to calculate the local flow speed using

$$U(X, Y) = \sqrt{\frac{2(p_{stag} - p_{stat})}{\alpha\rho_a + (1+\alpha)\rho_w}}. \tag{2.2}$$

Here α is the local void fraction, ρ_w is the density of water and ρ_a is the density of air determined using the ideal gas law with the local pressure and temperature. The accuracy of this flow speed measurement method decreases with increasing void fraction due to decreasing accuracy of the void fraction measurement and increasing potential for air in the pressure lines from the Pitot-static tubes. As there are nearly three orders of magnitude difference between the density of air and water, the computed velocity is extremely sensitive to the void fraction measurement. When propagating experimental uncertainties through (2.2), the velocity uncertainty increases rapidly with void fraction above ~0.5. In addition, the pressure measurement uncertainty increases with increasing void fraction due to the potential of air becoming trapped in the pressure lines. This added uncertainty impacts the velocity measurement primarily between void fractions of 0.2 and 0.8. Hence, the Pitot-static probe results are not reported although they were used at low void fractions as an independent estimate for measurement validation.

The gas (air) supply was particle filtered to ~10 μm upstream of three insertion thermal mass-flow meters (640S, Sierra Instruments) mounted in parallel for measuring the injection rate. The mass-flow meters were mounted at the centre of either a 6.3 or 7.8 cm inner diameter (ID) straight steel pipe. The three parallel measurement lines were combined within the injector manifold described by Elbing *et al.* (2011). The flow meters were positioned 30 IDs downstream and 10 IDs upstream of any line junctions to ensure that the flow was fully developed at the monitoring location. The sensors were factory calibrated over an operating range of 0–345 kPa and 10–54 °C from 0–0.45 and 0–0.56 kg s^{-1} for the 6.3 and 7.8 cm ID pipes, respectively. The accuracy was double checked at flow rates below 0.12 kg s^{-1} with a rotameter (Omega) and coincided within the accuracy of the rotameter (±0.002 kg s^{-1}). The mass-flow rate from each sensor was recorded simultaneously with the skin-friction data. Static pressure and tunnel water temperature were recorded simultaneously as well and were used to determine the local volume flux of air within the boundary layer.

The test model working surface was monitored continuously during testing with two high-speed cameras (piA640-210gm, Basler) and two low-speed cameras (scA750, Basler). The high-speed CCD cameras could acquire 648 × 488 pixel monochrome images at 210 fps. These cameras were mounted on the diagonal bottom chamfer of the LCC and were primarily used to monitor the flow near the traversing probes. The low-speed CMOS cameras could acquire 752 × 480 pixel images at 60 fps. These cameras were used primarily to monitor the working surface during data collection as it was difficult to see the test surface from the instrumentation control location. Image acquisition software (Streampix4, Norpix) controlled the collection and storage of images. The images were stored continuously on a 16 TB redundant array of independent disks (RAID), which was operated in the 1 + 0 configuration to achieve the data security and consistently fast read/write performance required for high-speed video streaming. In addition to this continuous monitoring system, separate cameras (D40, Nikon; EX-F1, Casio) were used to acquire still images and high-speed video for a subset of conditions.

Two laser-Doppler-velocimetry (LDV) systems were used to measure local velocities within the test section. The first LDV system, a stationary single-component LDV system described by Etter *et al.* (2005), acquired the streamwise velocity component at a single reference point located 5 cm upstream of the model leading edge and 31 cm below the test model centreline. The second LDV system, also described by Etter *et al.* (2005), was a traverse mounted two-component LDV system. The traversing LDV system was positioned to acquire the streamwise and wall-normal velocity components through the entire boundary layer at four streamwise locations ($X = 1.78, 2.09, 5.94$ and 9.94 m). Liquid velocity profiles were acquired with and without air injection. The free stream speed between LDV measurement locations downstream of the BFS was determined from static pressure measurements (PX2300-10DI, Omega), which were acquired on the model surface at $X = 2.59, 3.41, 5.09, 5.94, 6.61, 7.43, 9.23, 10.1, 10.7$ and 11.5 m. Measurements at all of these locations were acquired only for a subset of conditions. During testing the static pressure was recorded continuously for all conditions from either the model surface at $X = 2.59$ m or the tunnel wall at $(X, Y) = (3.95\text{ m}, 0.26\text{ m})$. It was used to determine the volumetric air flux from the mass-flux measurements.

2.4. *Test matrix*

The experimental program was conducted with the injection of air at a single free stream speed (U_∞) of nominally 6.3 m s^{-1}. Measurements of the wall skin friction, velocity profiles, static pressure and void fraction profiles were acquired from $X = 1.8$ to 11.5 m, which produced downstream-distance-based Reynolds numbers ($Re_X = U_\infty X/\nu$) to 8.1×10^7. The volumetric air injection rate varied between 0 and 1.1 m^3 s^{-1}. The average water temperature during testing was 25.2 ± 0.5 °C, leading to an average water density at 997 kg m^{-3} and an average kinematic viscosity (ν) of 8.9×10^{-7} m^2 s^{-1}. The test-matrix included experiments with and without VGs. When the VGs were used their AoA was 0, 5 or 10°. Skin friction and air flux were measured for all test conditions, while the velocity and traversing probe measurements were acquired for a subset of conditions.

3. Results and discussion

3.1. *Baseline*

With the current experimental setup a stable free surface could be established within the test section at LCC-impeller rotation rates from 10 to 17.5 rpm. The rotation rate was fixed at 17.5 rpm to achieve the highest Reynolds number and average free stream speed of 6.3 m s^{-1}. Owing to the BFS and boundary layer growth within the test section, the free stream speed varied along the model length (as shown in table 1). The local boundary layer thickness (δ) was determined from curve fitting the available experimental data for δ/X *versus* Re_X data collected downstream of the BFS. Table 1 includes the local free stream speed, boundary layer thickness, Reynolds number, friction velocity ($u_\tau = \{\tau_{wo}/\rho\}^{1/2}$) and wall unit ($l_\nu = \nu/u_\tau$) for each measurement location without air injection. The shear stress used to compute the friction velocity was determined from a power-law curve fit to measurements of the skin friction coefficient ($C_f = \tau_{wo}/0.5\rho U_\infty^2$) as a function of Re_X downstream of the BFS.

3.2. *Flow perturbations*

Following the convention used by Elbing *et al.* (2008), the critical air flux required to establish stable ALDR was defined as the flux required to achieve 80 % drag reduction.

X (m)	U_∞ (m s^{-1})	δ (mm)	Re_X $\times 10^6$	u_τ (m s^{-1})	l_ν (μm)	Measurements
1.8	6.42	30.8	12.8	—	—	LDV
2.1	6.23	60.8	14.6	—	—	LDV
3.4	6.29	72.9	24.1	0.21	4.3	SFB
3.6	6.30	74.2	25.3	0.21	4.3	TP
5.9	6.32	89.6	42.0	0.20	4.5	LDV, TP
7.4	6.34	97.6	52.9	0.19	4.6	SFB
9.2	6.36	106	66.0	0.19	4.7	SFB
9.9	6.37	109	71.2	0.19	4.7	LDV
10.6	6.38	111	76.1	0.19	4.7	TP
10.7	6.38	112	76.6	0.19	4.7	SFB

TABLE 1. Baseline (no-injection) parameters determined from the combination skin-friction and LDV measurements. Skin-friction data were not reported near the BFS location ($X = 2.0$) due to the location of the first skin-friction measurement ($X = 3.4$ m) and the presence of the BFS, preventing extrapolation with the fitted data. (LDV – laser Doppler velocimetry; SFB – skin-friction balance; TP – traversing probes).

Although arbitrary, this definition allows consistent comparisons. Alternative methods (e.g. peak in shear stress fluctuations) and alternative threshold values (85 and 90 %) revealed the same data trends. Owing to data scatter, the critical air flux measurements for each condition were determined from a linear fit to the measurements nominally spanning ±25 % of the critical air flux. In the absence of VGs, the air flux required to establish ALDR was approximately 0.036 m^2 s^{-1}, which is between that previously observed on a smooth (0.027 m^2 s^{-1}) and rough (0.040 m^2 s^{-1}) surface at the same flow speed without the BFS. However, the minimum flow speed tested in the previous study (Elbing *et al.* 2008) was 6.7 m s^{-1}; thus, as shown in figure 4, extrapolation of the previous data using a power-law fit was required to estimate the critical air flux at 6.3 m s^{-1}.

To investigate ALDR robustness, the incoming boundary layer was perturbed with the addition of a row of VGs, which were described previously. The VG AoA could be varied to change the induced strength of their vortical wakes. The influence of the VGs on the air layer is illustrated in figure 5, which shows two images produced from the average of 12 000 images acquired at 205 fps with the flow imaging system. The region shown is nominally 0.25–3.9 m downstream of the injection location with the protruding object in both views being the traversing probe system located at $X = 3.58$ m. The left image was acquired without VGs installed while the right image was acquired with VGs installed and set to 10° AoA. In the right image, the evenly spaced streaks correspond to trailing vortices from the VGs. Owing to optical access limitations a direct measurement of the vorticity near the BFS was not possible. However, it is possible to estimate VG wake circulation from the results of Yao *et al.* (2002), which were used to design the VGs. Linear interpolation between their low and conventional VG designs, combined with the observation by Yao *et al.* (2002) that the positive circulation is proportional to $\sin^{1.5}$(AoA) produce estimated positive circulations with the 5 and 10° AoA of 0.08 and 0.2 m^2 s^{-1} at the flow speed of these tests. As mentioned previously the VG design criterion was to produce sufficient circulation to induce a vertical velocity with sufficient kinetic energy to raise the air–water interface to the model surface. Although instrumentation limitations prevented a direct verification of such interface lifting, the right image in figure 5

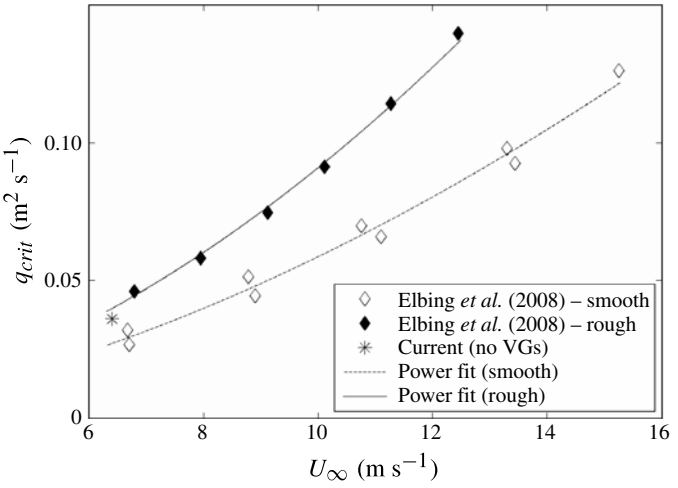

FIGURE 4. Comparison of the critical air flux required to establish ALDR with previous data collected on a smooth and a rough flat plate (Elbing *et al.* 2008). In the current experiment with the BFS, the required air flux is above that of the smooth flat plate but below that of the rough surface.

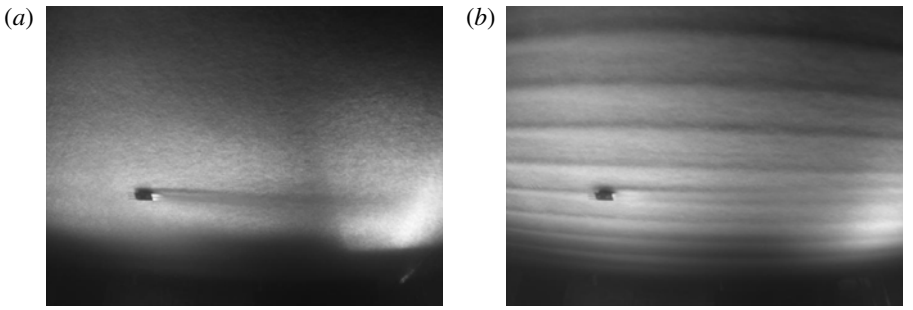

FIGURE 5. Averaged images of the test model working surface with an established air layer without (*a*) and with (*b*) VGs installed upstream of the BFS. The flow in both images is from left to right and nominally spans from 0.25 to 3.9 m downstream of the injection location. The object protruding from the bubbly boundary layer in each image is one of the traversing probe systems. The evenly spaced streaks in the right image correspond to vorticity streaks produced from individual VGs.

does confirm that the VGs at 10° AoA visibly altered the flow. However, based on qualitative observations presented by Elbing *et al.* (2008), it was thought that any such disturbances would result in the entire air layer becoming unstable, but these images show that this was not the case as the streaks remained confined behind the VGs.

With the VGs inserted immediately upstream of the BFS the critical air flux was 0.034, 0.035 and 0.043 m^2 s^{-1} when the VG AoA was 0, 5 and 10°, respectively. Of note, while the LCC's impeller rotation rate and pitch were fixed during testing, the initial fill height had minor variations that consequently caused variations in the free stream speed. As a result the average free stream speed with the AoA at 0 and 5° was 6.2 m s^{-1}, which could be the cause for the critical air fluxes being below

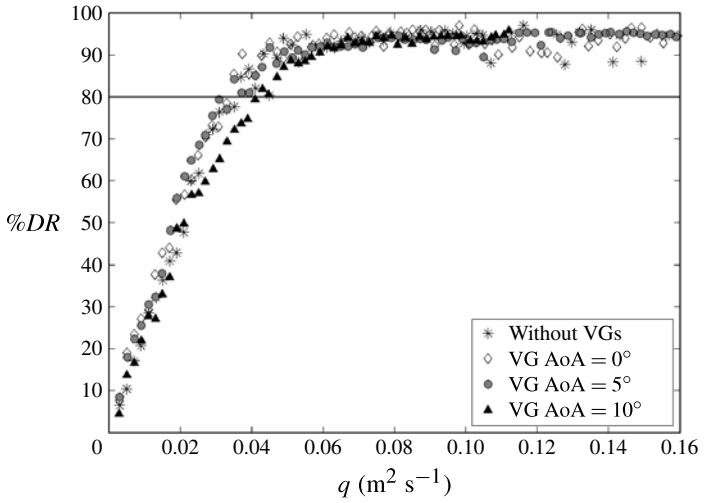

FIGURE 6. Per cent drag reduction versus the volumetric flux of air injected into the boundary layer. The solid line marks the 80 % criteria used by Elbing *et al.* (2008) to define the critical flux of air required to establish a stable air layer.

that observed with no VGs. The 10° AoA had approximately the same free stream speed as the non-VG condition, 6.3 m s^{-1}. Thus, to assess the small variations in critical air flux it is useful to compare them relative to the critical air flux on the smooth model, as determined from the power-law fit. Without VGs the air flux is 1.33 times the previous observed smooth model results while with VGs the air flux was 1.35, 1.38 and 1.62 times the smooth model results with the AoA at 0, 5 and 10°, respectively. Thus, a minimal increase in critical air flux was observed between the non-VG condition and VGs at an AoA of 0 and 5°. Conversely, an increase in the critical air flux (22 % relative to the non-VG condition) was observed when the AoA was increased to 10°. This sudden rise in VG influence between AoA 5 and 10° is intriguing. While there is insufficient data available to determine the cause, one possible explanation is that there may be a critical VG-wake circulation value that when exceeded has a destabilizing effect on the formation of an air layer.

These trends are illustrated in figure 6, which shows *%DR* as a function of the volumetric flux per unit span averaged over at least seven repeated gradual ramps in air flux. The figure shows that there is minimal variation in air flux required to achieve 80 % drag reduction between studies without VGs and VGs at 0 and 5° AoA. However, the increase is obvious at the 10° AoA condition. This suggests that the VG-wake circulation within the flow field causes an increase in the required air flux to establish a stable air layer. These results support the observation from Elbing *et al.* (2008) that the critical air flux is sensitive to the free stream turbulence level, but the use of a BFS at the injection location decreases the sensitivity expected by Elbing *et al.*

3.3. *Critical flux scaling*

Data reported in Elbing *et al.* (2008) showed that the critical flux of air required to transition to ALDR, q_{crit}, depends on free stream speed and surface roughness with increasing speed and roughness requiring larger fluxes, as shown in figure 4. As a first attempt to explain these dependencies, consider a single spherical bubble in the near-wall region of a shear flow and seek a simple description of how it might reach

the wall when buoyancy pushes it there. The goal here is merely to determine an appropriate scaling of the critical air flux for ALDR; thus the development provided here is qualitative as multiple-bubble phenomena and the influence of drag reduction prior to ALDR are ignored. In prior BDR research (Pal *et al.* 1989; Merkle & Deutsch 1990; Elbing *et al.* 2008), a region of near-zero void fraction was observed at the wall which has been attributed to the shear forces pulling bubbles from the solid surface. Following the work of Maxey & Riley (1983) and Magnaudet & Eames (2000), Sanders *et al.* (2006) provided the buoyancy force (F_B) to lift force (F_L) ratio,

$$\frac{F_B}{F_L} \approx \frac{2g}{(U_w - U_b)\,(\partial U_w/\partial Y)}, \tag{3.1}$$

as well as the buoyancy force to drag force (F_D) ratio,

$$\frac{F_B}{F_D} \approx \frac{R^2 g}{9\nu\,(V_w - V_b)}, \tag{3.2}$$

on a spherical bubble of radius R in a near-wall shear flow. Here g is gravitational acceleration, U_b and V_b are the bubble's velocity components in the streamwise, X, and wall-normal, Y, directions, respectively, and U_w and V_w are the water velocity components in the X and Y directions, respectively, in the absence of the bubble. The buoyancy force on the spherical bubble is $\rho_w g(4\pi R^3/3)$.

To determine the bubble's trajectory using Newton's second law, the bubble's apparent (or added) mass, $2\pi\rho_w R^3/3$ (see Kundu, Cohen & Dowling 2012), must be included. Apparent mass is critical when considering the dynamics of objects with a lower density than the fluid in which they are immersed. Thus, a simple Newton's second law statement in the wall-normal direction including the bubble mass is

$$\frac{\rho_w}{\rho_a}\left\{\frac{(U_w - U_b)}{2}\frac{\partial U_w}{\partial Y} + \frac{9\nu\,(V_w - V_b)}{R^2}\right\} + g\left(1 - \frac{\rho_w}{\rho_a}\right) = \left(1 + \frac{\rho_w}{2\rho_a}\right)\frac{\mathrm{d}V_b}{\mathrm{d}t}. \tag{3.3}$$

The shear rate ($\partial U_w/\partial Y$) varies within the boundary layer, but has a maximum at the wall for a flat plate turbulent boundary layer. Thus, as an upper bound for this simple analysis, the shear rate can be determined from the velocity profile within the viscous sublayer ($U^+ = Y^+$). Here $U^+(\equiv U/u_\tau)$ and $Y^+(\equiv Y/l_\nu)$ are the streamwise velocity and wall-normal direction scaled with inner variables, respectively. Consequently, the maximum shear rate in the near-wall region equals u_τ/l_ν. Inserting this shear rate into (3.3) and scaling the equation with inner variables (u_τ and l_ν, the '+' superscript indicates inner variable scaling) results in

$$\frac{\rho_w}{\rho_a}\left\{\frac{(U_w^+ - U_b^+)}{2} + \frac{9}{R^{+2}}(V_w^+ - V_b^+)\right\} + \left(1 - \frac{\rho_w}{\rho_a}\right)\frac{\nu g}{u_\tau^3} = \left(1 + \frac{\rho_w}{2\rho_a}\right)\frac{\mathrm{d}V_b^+}{\mathrm{d}t^+}. \tag{3.4}$$

Under ordinary atmospheric conditions, the density of water is nearly three orders of magnitude larger than air, which allows (3.4) to be approximated as a first-order, inhomogeneous linear differential equation,

$$\frac{\mathrm{d}V_b^+}{\mathrm{d}t^+} + \frac{18}{R^{+2}}V_b^+ = (U_w^+ - U_b^+) + \frac{18}{R^{+2}}V_w^+ - \frac{2\nu g}{u_\tau^3}. \tag{3.5}$$

Solving (3.5) for the vertical bubble velocity and applying the initial condition that the vertical velocity is some arbitrary value V_{bo}^{+} at time zero produces

$$V_b^+ = \left\{ \frac{(U_w^+ - U_b^+)}{18} R^{+2} + V_w^+ - \frac{\nu g}{9 u_\tau^3} R^{+2} \right\} (1 - \mathrm{e}^{-18t^+/R^{+2}}) + V_{bo}^+ \mathrm{e}^{-18t^+/R^{+2}}, \quad (3.6)$$

which can be evaluated using experimentally determined parameter values. Experimental results from Elbing *et al.* (2008) indicate that the bubble radius far from the injection location is typically of the order of 100 viscous wall units. In the current study a bubble released at the injection location has been in the flow for at least 0.22 s prior to reaching the first measurement location. This time combined with $R^+ \sim 100$ results in the exponential terms in (3.6) being on the order of 10^{-7} by the first measurement location (1.4 m downstream of the injection location). Thus, it is only necessary to consider the term in the braces (i.e. curly brackets) in (3.6). Consequently, the first bracketed term on the right-hand side of (3.6) must be negative for the bubble to rise to the surface ($V_b{}^+ < 0$). In addition, $V_w^+/R^{+2} \ll 1$ throughout equilibrium flat-plate boundary layers, so the two dominate factors inside the braces in (3.6) establish an inequality for the bubble to rise to the surface,

$$(U_w^+ - U_b^+) < \frac{2\nu g}{u_\tau^3}. \quad (3.7)$$

This inequality represents the imbalance between shear and buoyancy forces in the near-wall region necessary for a bubble to rise to the surface (i.e. form an air layer). Unfortunately, when there is relative velocity between the continuous and dispersed phases, the equations of motion cannot be solved as a mixture with average fluid properties but must be solved individually for each phase. This requires an understanding of the mass, force and energy interaction terms between phases, which are currently modelled by constructing heuristic models of the terms that are dependent on the given flow patterns (Brennen 2005). Thus, *a priori* knowledge of the flow topology is required to form the appropriate equations of motion, which makes an analytical solution for the relative velocity between the bubble and the water unlikely. However, the above inequality suggests that $\nu g/u_\tau^3$, which is readily available from the experimental measurements, may be an important scaling parameter for the occurrence of ALDR.

Using this parameter, results from the current study and from Elbing *et al.* (2008) with varying surface condition (smooth or fully rough), background surface tension (50 or 70 dyn cm^{-1}) and injector design (porous plate or slot) are provided in figure 7. Here, the critical air flux is scaled with the flux of liquid in the near-wall region, q_S, which Wu & Tulin (1972) approximated as 67.3ν. The friction velocities at the injection location were used for the smooth model data, which required extrapolation from the skin-friction measurements downstream of the injector. However, the surface roughness on the rough model was non-uniform downstream of the injection location so the friction velocity was determined from the average coefficient of friction along the model length. This scaling collapses the present measurements and the data from Elbing *et al.* (2008), and the empirical curve may be approximated with a power law:

$$\frac{q_{crit}}{q_s} = 6.135 \left(\frac{\nu g}{u_\tau^3} \right)^{-0.602}. \quad (3.8)$$

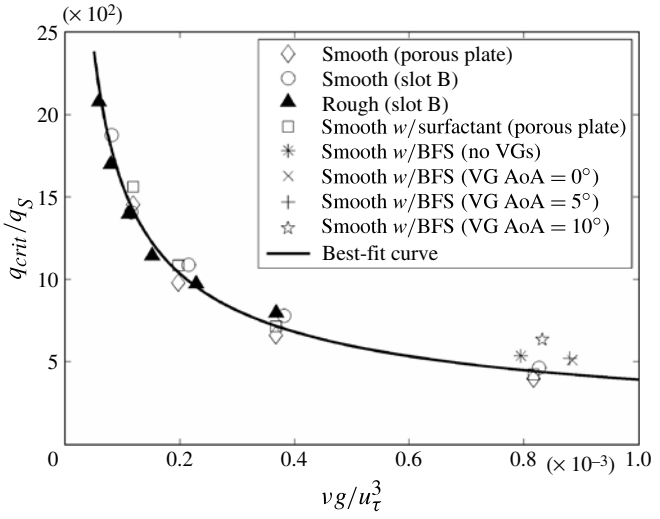

FIGURE 7. ALDR critical volumetric flux data from the current study and Elbing *et al.* (2008) scaled with the ratio of buoyancy to shear forces. Injection method, surface roughness and surface tension were varied.

Any air flux at or above this curve for a given $\nu g/u_\tau^3$ will result in ALDR. While this scaling collapses the available experimental ALDR data, it is a first approximation as it was developed from a limiting case that ignores bubble interactions for example.

With the exception of the 10° AoA condition, the results shown in figure 7 follow the power-law curve within the scatter of the data, though a slight bias toward higher volumetric fluxes may be evident for the current data. The 10° AoA condition (a single data point) exhibits a clear bias toward higher air flux for transition to ALDR that exceeds the scatter in the data. Of note is that the friction velocities with and without VGs were determined from the same friction curve. As a result it is difficult to assess the cause for this deviation. However, the streamwise VG-induced vorticity within the boundary layer increases the two cross-stream velocity components within the flow and these likely promote the diffusion of the bubbles. An additional explanation in the current study for the slight bias to higher volumetric fluxes for transition is the boundary layer disturbance created by the BFS, which was discussed previously. This will have minimal effect once the air layer is formed as the disturbance is reduced by the formation of an air layer, but it could possibly require larger amounts of air to initially form the air layer. If this were the cause a hysteresis effect would be observed, but this was not investigated during the current study. In spite of this minor deviation, the scaling does indicate that the critical volumetric air flux required for ALDR is primarily determined by balancing between shear-induced lift and buoyancy forces.

3.4. *Multiphase velocity profiles*

A significant complication introduced by the addition of a second phase into a turbulent flow is the possibility that the continuous and discrete velocity profiles are not equivalent. Consequently, it is necessary to independently measure the velocity profile for each phase. In the region where the void fraction is relatively low (i.e. the outer boundary layer) the liquid velocity profile was acquired with LDV. Results with air injection are compared with those acquired without air injection in figure 8.

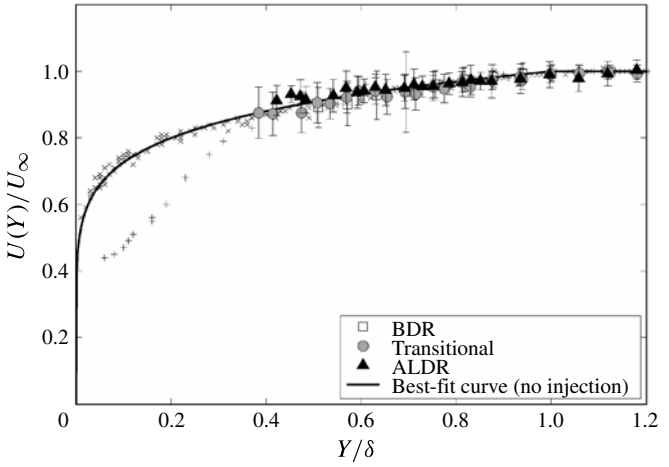

FIGURE 8. Liquid velocity profiles measured using LDV with and without air injection. The best-fit curve ($U/U_\infty = \{Y/\delta\}^{0.139}$) was produced from the no-injection data denoted by the symbol ($\times$), which correspond to points upstream or far downstream of the BFS. Data acquired with no injection near the reattachment point ($X = 0.09$ m) are also shown with ($+$) markers. Results with air injection were acquired at a single downstream position ($X = 5.94$ m) with and without VGs mounted upstream of the BFS.

The no-injection data denoted by ($\times$) include data from each VG configuration upstream and far downstream of the BFS. No-injection profiles acquired immediately downstream of the BFS ($+$) do not collapse on the best-fit curve provided in the plot (the near-wall velocity is suppressed relative to the profile shown). The data acquired with air injection were measured only at $X = 5.94$ m because this position was the closest that coincided with a traversing probe system. The data shown in figure 8 were acquired from a wide range of air injection volumetric fluxes (0.008–0.08 m^2 s^{-1}), which spanned the BDR, transitional and ALDR flow regimes. It is apparent from the figure that the liquid velocity with and without air injection are in agreement within the accuracy of the measurement (with air injection there is a significant increase in uncertainty). Thus, the liquid velocity profile is affected negligibly by the addition of air into the boundary layer when $Y/\delta = 0.4$. At this point it is unclear if the liquid velocity profile is altered in the near-wall region. However, it should be noted that the bubble velocity in the inequality provided in (3.7) was determined relative to the water velocity without the bubble present. This is not exactly the equivalent of the no-injection condition, but provides additional support for comparing the bubble velocity with the no-injection velocity profile.

The ToF sensors provide the interfacial velocity, which is assumed proportional to the gas-phase velocity. BDR conditions are analysed initially due to the BDR topology being well suited for ToF instrumentation, which require dispersed air–water interfaces. Current BDR interfacial velocity profiles are compared with the no-injection, single-phase velocity profile in figure 9. The BDR results were limited to conditions where $\%DR \leqslant 25$. There was negligible variation observed between profiles acquired at all three downstream positions ($X = 3.58$, 5.87 and 10.61 m), which indicates that the first measurement location was beyond the initial injection region. Thus, the profile for each VG configuration shown was produced from the average of the three streamwise profiles and spatially filtered in the wall-normal direction to improve clarity of the

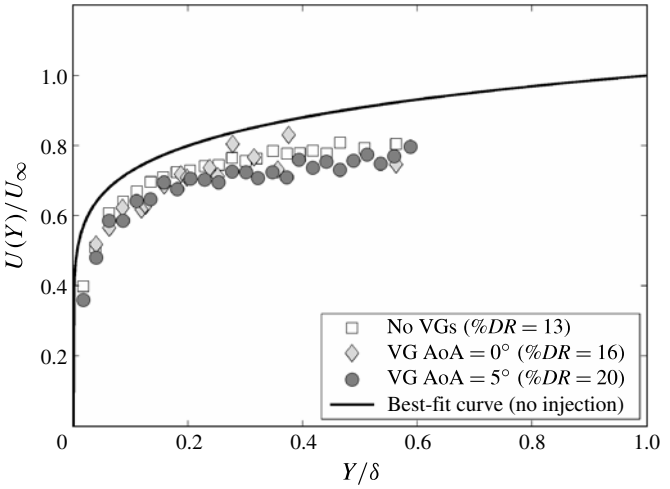

FIGURE 9. Interfacial velocity profiles during BDR ($\%DR = 25$) compared with the mean single-phase velocity profile. Shown are results from each VG configuration except 10°AoA, which had no data acquired for $\%DR = 25$. Each profile was determined by averaging data acquired from all three downstream positions. The no-injection free stream velocity and boundary layer thickness were used to scale the interfacial velocity.

trends. The no-injection free stream velocity and boundary layer thickness were used to scale the profiles. Included are profiles without VGs and with VGs at 0 and 5° AoA. Results from the 10° AoA were not included due to the minimum drag reduction condition measured being above $\%DR = 25$.

From figure 9 it is apparent that the interfacial velocity is suppressed relative to the single-phase velocity profile (noting that the liquid-phase velocity was unaltered relative to the no-injection condition in the outer boundary layer) and there is minimal variation between different VG configurations. Data were acquired further from the wall location, but the uncertainty increases significantly due to the lack of liquid/gas interfaces (this is supported subsequently with void fraction measurements). The suppressed interfacial velocity is expected since the gas–liquid interface allows for slip to occur, with the bubbles being dragged by the liquid.

The lowest air flux condition acquired with 10° VG AoA produced $\%DR \sim 35$. When scaled using outer variables the data from the three downstream positions collapsed. However, the collapsed profile followed the no-injection velocity profile with negligible variation rather than being suppressed like the other VG configurations. Unfortunately, given the limited scope of available data it is difficult to explain the cause for this observation at this level of drag reduction given that: the flow could be alternating between bubbly and an air layer; no other VG configuration was acquired at this $\%DR$; the 10° AoA-induced vorticity had a significant impact on the critical air flux relative to any other configuration; and there is likely significant spanwise non-uniformity in the flow (see figure 5). The issue of spanwise non-uniformity is a concern since the results will be sensitive to whether or not the probe lies in the vortical wake of one of the VGs.

From figure 6 it is apparent that the level of drag reduction, independent of the VG configuration, plateaus at a volumetric air flux of $\sim 0.06\ \mathrm{m^2\ s^{-1}}$. Thus, when investigating the interfacial ALDR velocity profiles only conditions with a

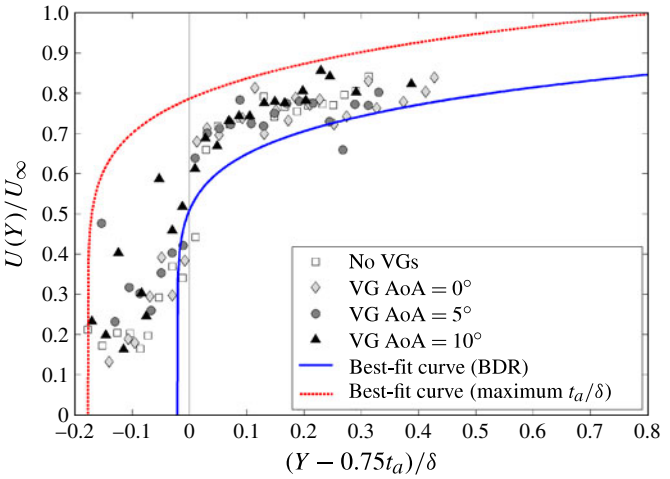

FIGURE 10. (Colour online) Interfacial velocity profiles during ALDR averaged from the three downstream positions for each VG configuration, and scaled with the nominal air layer thickness (t_a), free stream speed and no-injection boundary layer thickness. The average volumetric injection flux was 0.06 m^2 s^{-1}. Included for comparison is the no-injection best-fit curve scaled with the maximum t_a/δ value and a representative value for BDR conditions (U/U_∞ for the BDR condition was also multiplied by 0.87 to match data in figure 9).

volumetric flux above $\sim$0.06 m^2 s^{-1} were studied. Larger deviations between the gas-phase velocity and the interfacial velocity are expected with ALDR because the measurements within the air layer are associated primarily with slugs of bubbly mixture that randomly penetrate the air layer. The region beyond the air layer is a bubbly mixture with dispersed bubbles, which makes the interfacial velocity in that region more representative of the bubble velocity. When the BDR scaling used in figure 9 was applied to the ALDR conditions there was no apparent collapse of the data even though some trends emerged between certain conditions. Numerous scaling approaches were considered, but the scaling that led to the best collapse of the data was produced when it was assumed that the profile consisted of an air layer of some thickness with a bubbly mixture above the air layer. This assumption was further supported by void fraction measurements that show a layer of high void fraction ($\geqslant$0.85) followed by an abrupt drop to BDR-like void fraction levels as Y increases. Elbing *et al.* (2008) defined a length scale, t_a, that is the maximum air layer thickness if the air moves at the free stream speed ($t_a = q/U_\infty$), where q is the volumetric flux of air per unit span injected into the boundary layer. Investigation of the abrupt change in the void fraction and interfacial velocity profiles showed that in the current study the step change was consistently located at $0.75t_a$. The universality of this observation cannot be determined given the limited range of test conditions and use of a single BFS height, but this observation allows an empirical offset for scaling the velocity profiles for the current parameter range. Results averaged from the three downstream positions for each VG configuration are plotted in figure 10. Of note is that the results did show a slight dependence on downstream distance for a given VG configuration. In general, the velocity profile in the bubbly mixture above the air layer was shifted upward (to higher speeds) with increasing downstream distance. The trend may be the product of a significant decrease in the boundary layer thickness growth relative to that observed with the single-phase measurements (i.e. for far downstream distances the

boundary layer thickness used to scale would be larger than the actual boundary layer thickness). As the current experiment only measured the boundary layer thickness at a single downstream position with air injection, the validity of this suggestion could not be verified. Thus, for simplicity the profiles from the three downstream positions were averaged to make comparisons between VG configurations more apparent.

In general, the data collapse between VG configurations. There is an increase in the data scatter when $(Y - 0.75t_a)/\delta < 0$ (i.e. within the air layer) because the number of gas/liquid interfaces decreases, so that the number of interfacial velocity measurements decreases. In addition, the interfacial velocity may be more variable within the air layer. The average interfacial velocity within the air layer is approximately 20 % of the free stream velocity. Moreover, if it is assumed that the air layer thickness is defined such that $(Y - 0.75t_a)/\delta = 0$, then independent of downstream distance the air layer thickness was nominally 7 mm (slightly greater than half the BFS height). This is rather large given the observation of Elbing *et al.* (2008) that the air layer thickness was ∼1 mm (determined optically based on intensity of scattered light). It is difficult to make a comparison between measurements as the current results are more quantitative than those of Elbing *et al.* (2008), but the increased thickness is consistent with the observation that the BFS decreases the sensitivity to free stream turbulence (i.e. increasing air layer thickness increases the robustness of ALDR) and requires slightly larger fluxes of air to establish at a given free stream speed.

A complication associated with plotting the data in this manner is that the wall location varies with the volumetric flux of air. To help illustrate this point the best-fit curve for the no-injection velocity profile was scaled using a representative BDR condition ($t_a/\delta = 0.029$) and with the maximum value of t_a/δ tested ($t_a/\delta = 0.237$). The U/U_∞ for the BDR condition was also multiplied by a factor of 0.87 to match the results shown in figure 9. This shows that the interfacial velocity profile within the bubbly layer beyond the air layer is still suppressed relative to the no-injection condition. The overall picture of the interfacial velocity profile in the ALDR regime is that in the wall proximity the formation of an air layer shifts the boundary layer away from the wall. The shifted boundary layer flow behaves similar to that observed in the BDR regime, though the velocity is not as suppressed as observed in the BDR regime. This is due to the fact that the shifted boundary layer in the ALDR regime has a non-zero velocity at the air–water interface. These best-fit curves are also provided in figure 11, which shows the interfacial velocity profiles in the BDR, transitional ALDR and ALDR regimes. The BDR results closely follow the BDR scaled best-fit curve, as expected. For each condition with $Y > 0.75t_a$, the interfacial velocity profile is approximately equal to 0.87 times the no-injection velocity profile.

Finally the transitional ALDR regime is investigated by comparing the results using the ALDR scaling at various levels of drag reduction. Figure 11 shows the interfacial velocity profiles averaged from the three downstream positions and all the VG configurations at various levels of drag reduction. There are two profiles that correspond to transitional ALDR based on the definition established by Elbing *et al.* (2008), $\%DR = 40$ and $\%DR = 73$. It is apparent that the transitional data are more scattered compared with the BDR and ALDR results, which is due to the increased variability observed under these conditions (irregular fluctuations observed in the skin-friction measurements with time scales on the order of tens of seconds). However, it is also apparent that the transitional ALDR results follow the ALDR results within the scatter of the measurements. The profiles indicate that the typical air layer interfacial velocity profile is composed of: (i) a layer of nearly constant velocity equal to $\sim 0.2U_\infty$; (ii) a bubbly profile that has a power-law fit similar to that observed with the

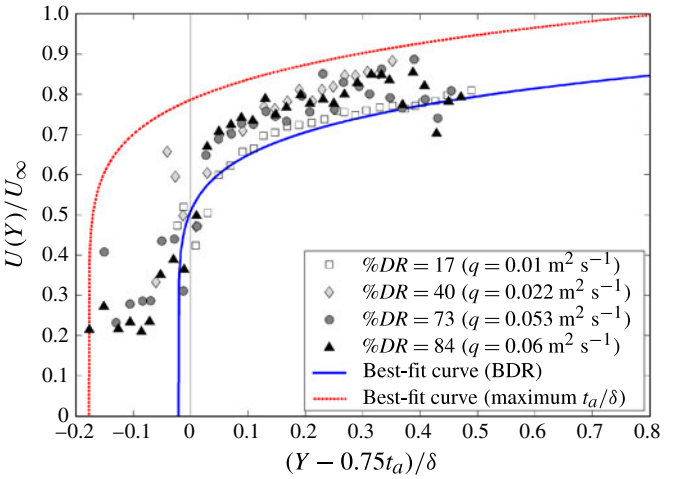

FIGURE 11. (Colour online) Interfacial velocity profiles for various levels of drag reduction determined from averaging the three downstream positions and all of the VG configurations. The velocity profiles were scaled following the ALDR results scaling. Once again, the no-injection best-fit curve scaled with the maximum t_a/δ value and a representative value for BDR conditions (U/U_∞ for the BDR condition was also multiplied by 0.87 to match data in figure 9) are included for comparison.

no-injection results and is positioned above $(Y - 0.75t_a)/\delta = 0$; and (iii) a nearly linear shear layer that transitions between the constant velocity layer and the power-law profile. This indicates that the transitional air layer is an air layer that forms, but is occasionally lost due to its insufficient thickness. The $\%DR = 40$ condition has the shear layer but lacks the layer of nearly constant velocity. This suggests that the near constant velocity layer is required for the layer to be sufficiently robust with respect to the boundary layer fluctuations. Thus, the per cent drag reduction in the transitional ALDR regime is essentially a measure of the percentage of time that the air layer is disturbed by the turbulent flow.

3.5. *Void fraction profiles*

The void fraction profiles are more difficult to assess due to their decreased accuracy relative to the other measurements presented. With the exception of the near-wall measurements, void fraction uncertainty is approximately 10 %. The near-wall uncertainty is larger due to the influence of the metal surface on the electrical circuit. As noted earlier the influence volume is less than 2 mm, thus the minimum position reported was 4 mm from the wall. However, the increased uncertainty typically extends to approximately $Y/\delta \sim 0.1$. In addition, the electrical impedance point probe circuit from the traverse positioned at $X = 5.9$ m was inadvertently altered during testing, which has required all subsequent results to be omitted herein. In spite of these limitations, the void fraction measurements are valuable due to the dearth of available data within the literature, especially at higher Reynolds numbers. Furthermore, the combined void fraction and velocity profiles allow conservation-law checks that increase confidence in the findings.

Similar to the interfacial velocity profiles, the discussion of the void fraction will begin with the BDR results ($\%DR = 25$). This flow topology has the advantage of having a flow field that, at least far from the wall, can be treated as a homogeneously

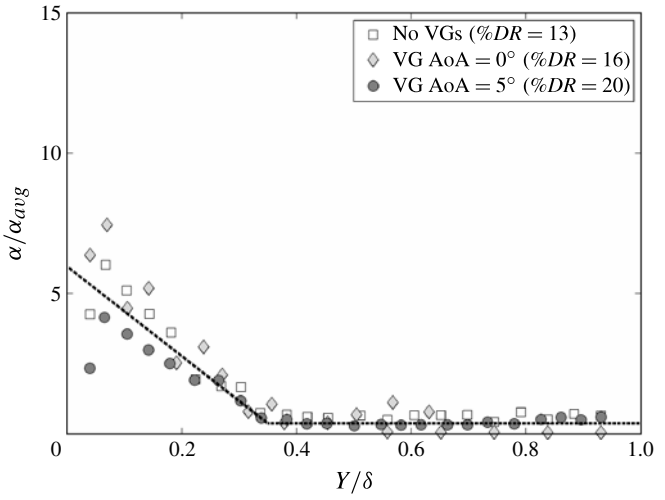

FIGURE 12. Local void fraction (α) profiles scaled with the single-phase boundary layer thickness and the average void fraction within the boundary layer (α_{avg}). Shown are the average profiles from the three downstream positions for each VG configuration with the exception of the 10° AoA condition, which did not have a measurement with $\%DR \leqslant 25$. The dashed line is a first-order approximation estimated from the total volumetric flux and the BDR bubble velocity profile.

dispersed mixture, which justifies the use of the Maxwell mixture model (Hewitt 1978; Ceccio & George 1996; Cho, Perlin & Ceccio 2005). However, it should be noted that the BDR results were processed independently assuming stratified and dispersed flow topologies and that both approaches produced similar results. By inspection and subsequent analysis, the void fraction profiles from the three downstream positions collapsed, within the accuracy of the measurement, by scaling the void fraction with the single-phase boundary layer thickness and the average void fraction within the boundary layer,

$$\alpha_{avg} = \frac{q}{q + U_\infty (\delta - \delta^*)}. \tag{3.9}$$

Here δ^* is the boundary layer displacement thickness, which is nominally equal to $\delta/8$ since the velocity profile in the current study is well approximated by the typical 1/7th power-law fit. Results from each VG configuration with the exception of the 10° AoA condition (minimum %DR acquired was above 25) are provided in figure 12. Unexpectedly, given that the drag reduction and velocity profiles collapsed, the curves do not collapse between VG configurations. This spread is most likely a measure of the increasing uncertainty as one approaches the wall rather than a revelation about the flow physics. This is as assumed because the scatter in the 0° AoA condition nearly spans the other profiles, and it was this condition that had the fewest recorded measurements. In spite of this limitation, these results definitely show that for $Y/\delta > 0.35$ there is a low but constant void fraction through the boundary layer thickness. Furthermore, there is evidence that the void fraction peaks away from the wall as the first measurement location is consistently lower than the second. This is consistent with previous research (Pal *et al.* 1989; Merkle & Deutsch 1990;

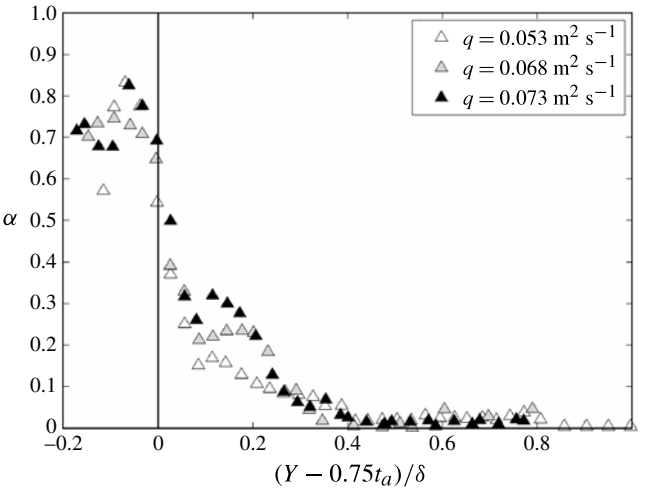

FIGURE 13. Local ALDR void fraction profiles scaled with the single-phase boundary layer thickness and the nominal air layer thickness (t_a). The profiles shown were produced from averaging the results from the three downstream positions and each VG configuration for a fixed range of volumetric injection fluxes. The average per cent drag reduction for each profile shown was between 80 and 100.

Elbing *et al.* 2008), which found that the peak void fraction is located away from the wall and that there is a region of near-zero void fraction at the wall.

An approximate overall validation check of the void fraction and velocity profiles is possible since the integral of their product through the boundary layer thickness should equal the total volumetric flux of air. Here simple fitted functional relationships for the void fraction and velocity profiles are used to avoid the uncertainty produced from numerically integrating scattered experimental data points. Hence, the velocity profile is approximated using the single-phase velocity profile multiplied by a factor of 0.87, which well approximates the results shown in figure 9. For simplicity the void fraction profile was approximated as piecewise linear from the results shown in figure 12. For $Y/\delta = 0.35$ the profile is nearly constant with $\alpha/\alpha_{avg} = 0.355$ (corresponds to a void fraction between 0.5 and 1.5 %), and for $Y/\delta < 0.35$ the profile intersects at the point (0.35, 0.355) and has a negative slope of a value to be determined. Integration of the product and the requirement that it must equal the total volumetric flux produces the required void fraction slope for $Y/\delta < 0.35$. The resulting piecewise linear profile is included in figure 12. The experimental data are scattered around the fitted profile, and this provides an approximate overall validation of the void fraction and velocity profiles. However, this simple integral analysis assumes that the fluctuating components of streamwise velocity and void fraction are uncorrelated. Given that Nagaya *et al.* (2001) experimentally observed that the streamwise velocity fluctuations increased with increasing air volume flux, they are correlated to some degree. However, in the same study it was also suggested that the air must decorrelate velocity fluctuations as the Reynolds stress decreases in spite of the increased fluctuations, which supports the implicit assumption in the mean-profile integral analysis presented here.

The ALDR void fraction profiles are provided in figure 13 and are significantly different from the BDR results. The ALDR void fraction profile has an abrupt change

in void fraction at $Y = 0.75t_a$. Owing to the nearly constant void fraction within the air layer (i.e. $Y < 0.75t_a$), the void fraction profiles were not scaled with the average void fraction as was done with the BDR results. As the void fraction within the air layer is independent of the injection flux, scaling with the average void fraction actually decreases the correlation. In addition, graphing the results with the scaling shown in figure 13 clearly reveals that the air layer thickness is approximately $0.75t_a$. This observed jump in void fraction clearly differs from the linear decline in void fraction observed during BDR (see figure 12), and highlights the difference in flow topology between BDR and ALDR. It is also important to note that the void fraction measurements within the air layer are biased to lower void fractions due to the measurement technique being designed for void fraction levels below ~0.5. When the data were processed using only the stratified topology assumption, the resulting profiles were similar in shape with a higher void fraction (~0.85) within the air layer and larger scatter. These results demonstrate that the air layer thickness increases with increasing volumetric injection flux. Thus, there is negligible variation in profile shape within the air layer with increasing air flux, though the increased air flux is more resilient to disturbances within the boundary layer.

Comparison between VG configurations and downstream locations did not reveal any apparent trend besides a dependence on the volumetric flux used to achieve the air layer. Thus the profiles shown in figure 13 were averaged among all VG configurations and downstream positions for a given range of volumetric fluxes. Provided in the legend is the average volumetric flux for each profile, when each had a resulting average per cent drag reduction between 80 and 100. The resulting profiles are nearly constant for $(Y - 0.75t_a)/\delta < 0$ and $(Y - 0.75t_a)/\delta \geqslant 0.4$. The void fraction within the air layer ($Y < 0.75t_a$) is nominally 0.75, and the void fraction in the outer region of the boundary layer ($(Y - 0.75t_a)/\delta \geqslant 0.4$) is approximately 0.02. Results for $(Y - 0.75t_a)/\delta \geqslant 0.8$ decrease to nearly zero void fraction, which is consistent with a boundary layer thickness abscissa value between 0.87 and 0.96 in the current study. The region between the air layer and the outer boundary layer region ($0 < (Y - 0.75t_a)/\delta < 0.4$) appears to be composed of a family of curves dependent on the given volumetric flux. This is expected as integration of the product of the ALDR velocity profile (figure 10) and the void fraction profile (figure 13) to determine the total volumetric injection flux, produces a void fraction curve dependent on the volumetric flux, free stream speed and boundary layer thickness (i.e. average void fraction). As the void fraction is independent of the injection condition with the exception of the region $0 < (Y - 0.75t_a)/\delta < 0.4$, it is this region that must be dependent on the average void fraction. This is further supported because the data, when scaled with the average void fraction in this region, collapse reasonably well.

Finally, the transitional ALDR void fraction profiles are investigated by plotting the mean void fraction profiles scaled with the average void fraction within the boundary layer (α_{avg}) in figure 14. While this method scatters further the results within the air layer, it reveals the trend between the various drag reduction regimes. The BDR void fraction profile is shifted towards the outer region of the boundary layer relative to that of the ALDR profiles. This observation is consistent with the 'liquid layer' reported by Pal *et al.* (1989). The liquid layer observed had no bubbles within the viscous sublayer region, which indicates that the void fraction in the near-wall region is zero. Consequently, it is expected that the BDR void fraction would be shifted away from the wall. Thus the transitional ALDR void fraction profile falls between the BDR and ALDR void fraction curves. As the volumetric flux increases and consequently the drag reduction also increases, the void fraction profile converges to the ALDR profile.

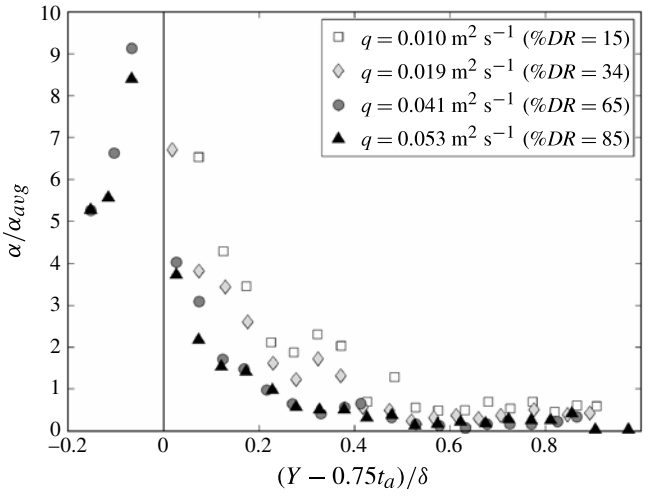

FIGURE 14. Mean void fraction profiles for various levels of drag reduction scaled with the average void fraction, air layer thickness and the single-phase boundary layer thickness.

This indicates that the transitional ALDR condition most likely represents irregularly alternating between BDR and ALDR.

4. Summary and conclusions

In the current study the various regimes of air-induced drag reduction were examined on a 12.9 m long flat-plate test model modified with the addition of a 13 mm BFS at the injection location. Testing was performed at a single free stream speed (6.3 m s^{-1}) with and without vortex generators used to perturb the incoming boundary layer. Previous ALDR critical volumetric flux results were scaled with the free stream speed in Elbing *et al.* (2008), which failed to collapse results when varying the surface roughness. The current study required air fluxes between the previous smooth and fully rough surface results to create an air layer. A potential scaling for the critical air flux was developed by analysing a single bubble subjected to a shear flow. This scaling indicates that the transition to ALDR depends on the ratio of buoyancy to turbulent shear forces ($\nu g/u_\tau^3$), and is successful for current and past (Elbing *et al.* 2008) experimental ALDR data. The buoyancy force promotes phase separation while turbulent fluctuations enhance phase dispersion. Although it is based on elementary analysis, the suggested scaling does collapse results from varying flow speeds with different surface conditions (smooth and fully rough), background surface tension and air injection designs. The only result that exhibited significant deviation from this scaling was with VGs at a 10° AoA, which required a higher air flux than predicted. This suggests that the friction velocity used as a characteristic dispersion velocity was insufficient or inappropriate for this condition. Thus, the dispersion velocity should likely also take into account the VG-induced circulation within the boundary layer. In general, the proposed scaling is likely a good starting point for future work on ALDR phenomenon, which is sensitive to upstream flow perturbations but the sensitivity decreases with the use of a clean separation line at the point of injection.

Owing to the relative dearth of void fraction and gas-phase velocity profile measurements in the literature, an effort was made to revisit BDR with a traversing

probe system. The wall-normal direction was scaled with the boundary layer thickness for both the void fraction and the interfacial velocity profiles. The void fraction was scaled with the average void fraction within the boundary layer, while the gas phase velocity profile was scaled with the free stream speed. Unfortunately, measurements in the BDR regime were not acquired with the VG 10° AoA configuration, which would have been informative regarding the deviation in the critical volumetric air flux scaling. However, measurements were acquired for the other VG configurations. Although suppressed the interfacial velocity had a similar shape to the single-phase velocity profile, independent of the VG configuration. This is expected as the bubble is dragged by the liquid phase and a slip boundary condition exists between the gas and liquid phases. The void fraction profiles showed deviation among various VG configurations, but this scatter is likely due to measurement uncertainty increasing near the wall. This assumption was supported by the lack of an observed trend in the measurement scatter and integration of the product of the velocity and void fraction profiles.

Scaling of the ALDR void fraction and interfacial velocity profiles was more complicated than the BDR results. ALDR results did not collapse using the BDR scaling approach. Thus, empirical scalings were explored and those that exhibited the best collapse of the collected data are presented. The scaling used herein was deduced by assuming that when an air layer was present the boundary layer consisted of an air layer (of thickness proportional to the injection flux) and a bubbly mixture beyond the air layer. Both the void fraction and the velocity profiles showed an abrupt change at nominally $0.75t_a$, where $t_a = q/U_\infty$ is an outer-scale air layer thickness. This abrupt transition was different from that observed during BDR. Within the air layer ($Y < 0.75t_a$), the void fraction was nearly constant at approximately 0.75, and the interfacial velocity profile was nearly constant at nominally $0.2U_\infty$. The bubbly mixture beyond the air layer ($Y > 0.75t_a$) was assumed to exhibit a behaviour similar to that observed with BDR. This assumption was validated by the interfacial velocity profile scaling with the free stream speed and the void fraction scaling with the average void fraction within the boundary layer. A thin shear layer exists between the air layer and the bubbly mixture. Of note, when the minimum air flux for ALDR is used the constant velocity region within the air layer is not observed even though the thin shear layer is present. Thus, increasing air flux increases the air layer thickness, which makes the air layer more resistant to local perturbations that could disturb the air layer.

Investigation of the velocity and void fraction profiles in the transitional regime indicates that the transitional regime is composed of alternating formation and breakdown of an air layer. The per cent drag reduction within the transitional regime was determined based on the percentage of time that an air layer was present. This was supported by the void fraction and velocity profiles in the transitional ALDR regime. While the interfacial velocity profiles were similar to the ALDR profiles, investigation showed that the transitional ALDR profiles lacked the region of constant velocity observed within the ALDR profiles. The void fraction profiles appeared to have a more gradual transition between the BDR and ALDR profiles in proportion to the level of drag reduction. Thus, a more appropriate terminology for the transitional regime would be either transitional ALDR or intermittent air layer regime.

Acknowledgements

The authors would like to thank the technical staff of the US Navy's W. B. Morgan Large Cavitation Channel, especially Mr R. Etter. We would also like to honour the

memory of Mr B. Hornaday, the LCC safety officer and former director. Such a large experiment could not have been possible without help with machining and fabrication of the test components (Mr K. Pruss, Mr W. Kirkpatrick and Mr D. Parsons) and execution of the experiment (Dr S. Zalek, Dr K. Lay and Mr R. Mooney). This research was sponsored by ONR under Contract N00014-08-1-0215 (Dr L. P. Purtell, Program Manager). The content of this document does not necessarily reflect the position or the policy of the US Government, and no official endorsement should be inferred.

REFERENCES

AMROMIN, E., KOPRIVA, J., ARNDT, R. E. A. & WOSNIK, M. 2006 Hydrofoil drag reduction by partial cavitation. *Trans. ASME: J. Fluids Engng* **128** (5), 931–936.

BODGEVICH, V. G. & EVSEEV, A. R. 1976 The distribution of skin friction in a turbulent boundary layer of water beyond the location of gas injection. In *Investigations of Boundary Layer Control*, p. 62. Thermophysics Institute Publishing House (in Russian).

BRENNEN, C. E. 2005 *Fundamentals of Multiphase Flow*. Cambridge University Press.

CECCIO, S. L. 2010 Friction drag reduction of external flows with bubble and gas injection. *Annu. Rev. Fluid Mech.* **42**, 183–203.

CECCIO, S. L. & GEORGE, D. L. 1996 A review of electrical impedance techniques for the measurement of multiphase flows. *J. Fluids Engng* **118**, 391–399.

CHO, J., PERLIN, M. & CECCIO, S. L. 2005 Measurements of near-wall stratified bubbly flows using electrical impedance. *Meas. Sci. Technol.* **16** (4), 1021–1029.

DAVIS, A. M. J. & LAUGA, E. 2010 Hydrodynamic friction of Fakir-like superhydrophobic surfaces. *J. Fluid Mech.* **661**, 402–411.

DRUZHININ, O. A. & ELGHOBASHI, S. 1998 Direct numerical simulations of bubble-laden turbulent flows using two-fluid formulation. *Phys. Fluids* **10**, 685–697.

ELBING, B. R., WINKEL, E. S., LAY, K. A., CECCIO, S. L., DOWLING, D. R. & PERLIN, M. 2008 Bubble-induced skin-friction drag reduction and the abrupt transition to air-layer drag reduction. *J. Fluid Mech.* **612**, 201–236.

ELBING, B. R., WINKEL, E. S., CECCIO, S. L., PERLIN, M. & DOWLING, D. R. 2010 High-Reynolds-number turbulent-boundary-layer wall pressure fluctuations with dilute polymer solutions. *Phys. Fluids* **22**, 085104.

ELBING, B. R., SOLOMON, M. J., PERLIN, M., DOWLING, D. R. & CECCIO, S. L. 2011 Flow-induced degradation of drag-reducing polymer solutions within a high-Reynolds-number turbulent boundary layer. *J. Fluid Mech.* **670**, 337–364.

ETTER, R. J., CUTBIRTH, J. M., CECCIO, S. L., DOWLING, D. R. & PERLIN, M. 2005 High Reynolds number experimentation in the U.S. Navy's William B. Morgan large cavitation channel. *Meas. Sci. Technol.* **16** (9), 1701–1709.

FERRANTE, A. & ELGHOBASHI, S. 2004 On the physical mechanisms of drag reduction in spatially developing turbulent boundary layer laden with microbubbles. *J. Fluid Mech.* **503**, 345–355.

HEWITT, G. F. 1978 *Measurement of Two-Phase Flow Parameters*. Academic.

KIM, J., KLINE, S. J. & JOHNSTON, J. P. 1980 Investigation of reattaching turbulent shear layer: flow over a backward-facing step. *Trans. ASME: J. Fluid Engng* **102**, 302–308.

KLEWICKI, J. C. 2010 Reynolds number dependence, scaling, and dynamics of turbulent boundary layers. *Trans. ASME: J. Fluids Engng* **132** (9), 094001.

KODAMA, Y., KAKUGAWA, A. & TAKAHASHI, T. 1999 Preliminary experiments on microbubbles for drag reduction using a long flat plate ship, *ONR Workshop on Gas Based Surface Ship Drag Reduction (Newport, USA)*, 1–4.

KODAMA, Y., KAKUGAWA, A., TAKAHASHI, T. & KAWASHIMA, H. 2000 Experimental study on microbubbles and their applicability to ships for skin friction reduction. *Intl J. Heat Fluid Flow* **21**, 582–588.

KODAMA, Y., KAKUGAWA, A., TAKAHASHI, T., NAGAYA, S. & SUGIYAMA, K. 2002 Microbubbles: drag reduction mechanism and applicability to ships, *24th Symposium on Naval Hydrodynamics*, 1–19. The National Academies Press.

KODAMA, Y., HORI, T., KAWASHIMA, M. M. & HINATSU, M. 2006 A full scale microbubble experiment using a cement carrier, *European Drag Reduction and Flow Control Meeting, Ischia, Italy*, 1–2.

KONRAD, J. 2011 The bubble ship – Mitsubishi's new green ship technology, *gCaptain*, Unofficial Networks, October 24, http://www.gcaptain.com.

KUNDU, P. K., COHEN, I. M. & DOWLING, D. R. 2012 *Fluid Mechanics*, 5th edn. pp. 236–240 Elsevier.

LAY, K. A., YAKUSHIJI, R., MÄKIHARJU, S., PERLIN, M. & CECCIO, S. L. 2010 Partial cavity drag reduction at high Reynolds numbers. *J. Ship Res.* **54** (2), 109–119.

LEE, C. & KIM, C. J. 2011 Underwater restoration and retention of gases on superhydrophobic surfaces for drag reduction. *Phys. Rev. Lett.* **106** (1), 014502.

LU, J., FERNÁNDEZ, A. & TRYGGVASON, G. 2005 The effect of bubbles on the wall drag of a turbulent channel flow. *Phys. Fluids* **17**, 095102.

LUMLEY, J. L. 1973 Drag reduction in turbulent flow by polymer additives. *J. Polym. Sci., Macromolecular Rev.* **7**, 283–290.

LUMLEY, J. L. 1977 Drag reduction in two phase and polymer flows. *Phys. Fluids* **20**, S64–S70.

MADAVAN, N. K., DEUTSCH, S. & MERKLE, C. L. 1985 Measurements of local skin friction in a microbubble modified turbulent boundary layer. *J. Fluid Mech.* **156**, 237–256.

MAGNAUDET, J. & EAMES, I. 2000 The motion of high-Reynolds-number bubbles in inhomogeneous flows. *Annu. Rev. Fluid Mech.* **32**, 659–708.

MÄKIHARJU, S. 2012 The dynamics of ventilated partial cavities over a wide range of Reynolds numbers and quantitative 2D X-ray densitometry for multiphase flow, PhD thesis, University of Michigan.

MARTELL, M. B., PEROT, J. B. & ROTHSTEIN, J. P. 2009 Direct numerical simulations of turbulent flows over superhydrophobic surfaces. *J. Fluid Mech.* **620**, 31–41.

MATVEEV, K. I., BURNETT, T. J. & OCKFEN, A. E. 2009 Study of air-ventilated cavity under model hull on water surface. *Ocean Engng* **36** (12–13), 930–940.

MATVEEV, K. I. & MILLER, M. J. 2011 Air cavity with variable length under a model hull. *Proc. IMechE M: J. Engng Maritime Environ.* **225**, 161–169.

MAXEY, M. R. & RILEY, J. J. 1983 Equation of motion for a small rigid sphere in a non-uniform flow. *Phys. Fluids* **26**, 883–889.

MCCORMICK, M. E. & BATTACHARYYA, R. 1973 Drag reduction of a submersible hull by electrolysis. *Naval Engrs J.* **85**, 11–16.

MENG, J. C. S. & UHLMAN, J. S. 1998 Microbubble formation and splitting in a turbulent boundary layer for turbulence reduction, *Proceedings of the International Symposium on Seawater Drag Reduction*, 341–355.

MERKLE, C. & DEUTSCH, S. 1990 Drag reduction in liquid boundary layers by gas injection. In *Viscous Drag Reduction in Boundary Layers* (ed. D. M. Bushnell & J. N. Hefner), *Progress in Astronautics and Aeronautics*, 123. pp. 351–412. AIAA.

MERKLE, C. & DEUTSCH, S. 1992 Microbubble drag reduction in liquid turbulent boundary layers. *Appl. Mech. Rev.* **45** (3), 103–127.

NAGAMATSU, T., KODAMA, T., KAKUGAWA, A., TAKAI, M., MURAKAMI, K., ISHIKAWA, H., KAMIIRISA, S., OGIWARA, Y., YOSHIDA, T., SUZUKI, Y., TODA, H., KATO, A., IKEMOTO, S., YAMATANI, S., IMO, K. & YAMASHITA, 2002 A full-scale experiment on microbubbles for skin friction reduction using SEIUN MARU. Part 2. The full-scale experiment. *J. Soc. Nav. Archit. Japan* **192**, 15–28.

NAGAYA, S., KAKUGAWA, A., KODAMA, Y. & HISHIDA, K. 2001 PIV/LIF measurements on 2-D turbulent channel flow with microbubbles, *4th International Symposium on PIV, Goettingen, Germany*.

OWEIS, G. F., WINKEL, E. S., CUTBRITH, J. M., CECCIO, S. L., PERLIN, M. & DOWLING, D. R. 2010 The mean velocity profile of a smooth-flat-plate turbulent boundary layer at high Reynolds number. *J. Fluid Mech.* **665**, 357–381.

PAL, S., DEUTSCH, S. & MERKLE, C. L. 1989 A comparison of shear stress fluctuation statistics between microbubble modified and polymer modified turbulent flow. *Phys. Fluids* **A1**, 1360–1362.

ROTHSTEIN, J. P. 2010 Slip on superhydrophobic surfaces. *Annu. Rev. Fluid Mech.* **42**, 89–109.

SANDERS, W. C., WINKEL, E. S., DOWLING, D. R., PERLIN, M. & CECCIO, S. L. 2006 Bubble friction drag reduction in a high-Reynolds-number flat-plate turbulent boundary layer. *J. Fluid Mech.* **552**, 353–380.

VAN DEN BERG, T. H., LUTHER, S., LATHROP, D. P. & LOHSE, D. 2005 Drag reduction in bubbly Taylor–Couette turbulence. *Phys. Rev. Lett.* **94**, 044501.

WATANABE, O., MASUKO, A. & SHIROSE, Y. 1998 Measurements of drag reduction by microbubbles using very long ship models. *J. Soc. Nav. Archit. Japan* **183**, 53–63.

WHITE, C. M. & MUNGAL, M. G. 2008 Mechanics and prediction of turbulent drag reduction with polymer additives. *Annu. Rev. Fluid Mech.* **40**, 236–256.

WINKEL, E. S., OWEIS, G., VANAPALLI, S. A., DOWLING, D. R., PERLIN, M., SOLOMON, M. J. & CECCIO, S. L. 2009 High Reynolds number turbulent boundary layer friction drag reduction from wall-injected polymer solutions. *J. Fluid Mech.* **621**, 259–288.

WU, J. & TULIN, M. P. 1972 Drag reduction by ejecting additive solutions into pure-water boundary layer. *Trans. ASME: J. Basic Engng* **94**, 749–756.

YAO, C.-S., LIN, J. C. & ALLAN, B. G. 2002 Flow-field measurement of device-induced embedded streamwise vortex on a flate plate, *1st AIAA Flow Control Conference, St Louis, MO*, Paper 2002-3162.